ISCI, Volume *23*

Supplemental Information

A Co-Doped Nanorod-like RuO_2 Electrocatalyst with Abundant Oxygen Vacancies for Acidic Water Oxidation

Yuanyuan Tian, Shuo Wang, Ever Velasco, Yueping Yang, Lujie Cao, Linjuan Zhang, Xing Li, Yichao Lin, Qiuju Zhang, and Liang Chen

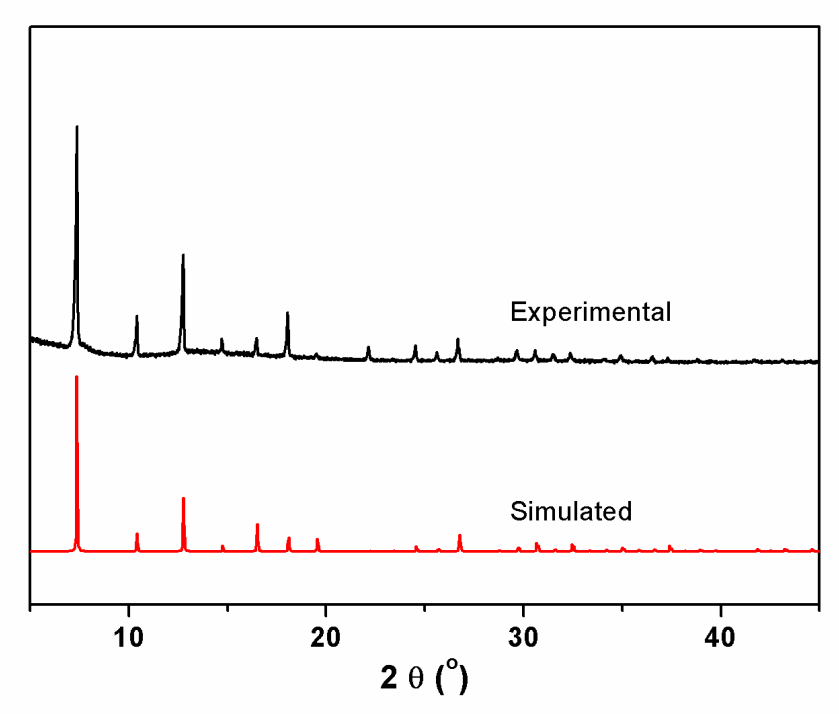

Figure S1. PXRD pattern of as-prepared ZIF-67. Related to Scheme 1.

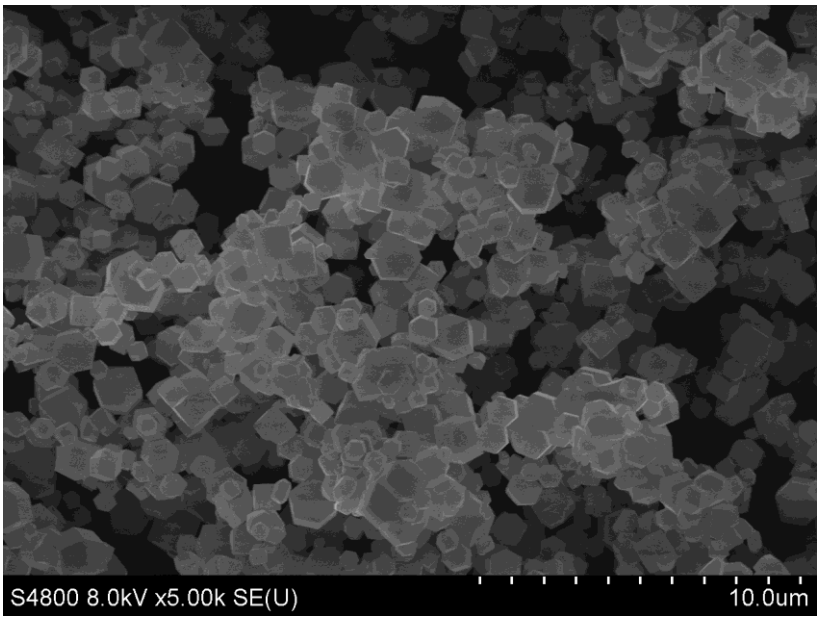

Figure S2. SEM image of as-prepared ZIF-67. Related to Scheme 1.

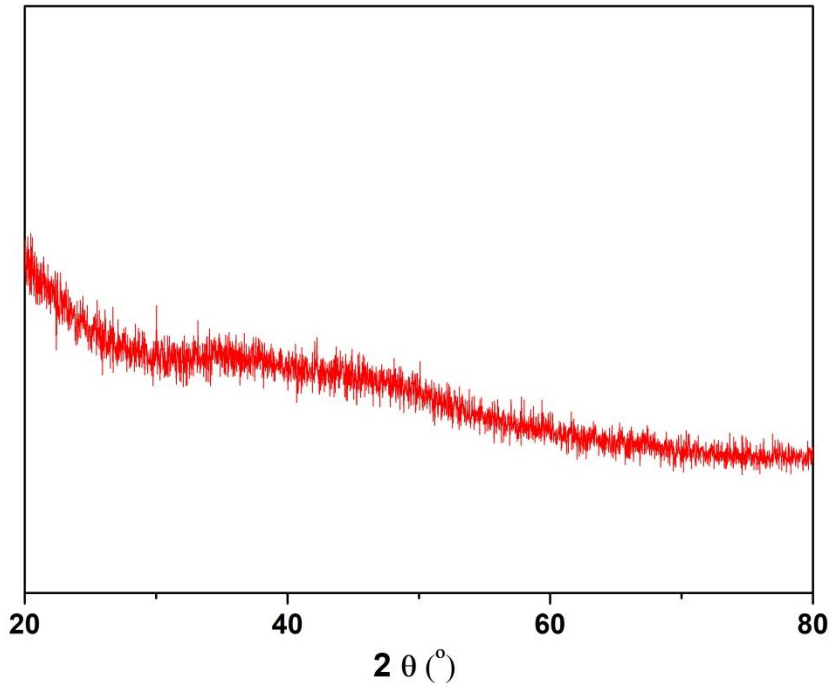

Figure S3. PXRD pattern of Ru-ZIF-67-C. Related to Figure 1.

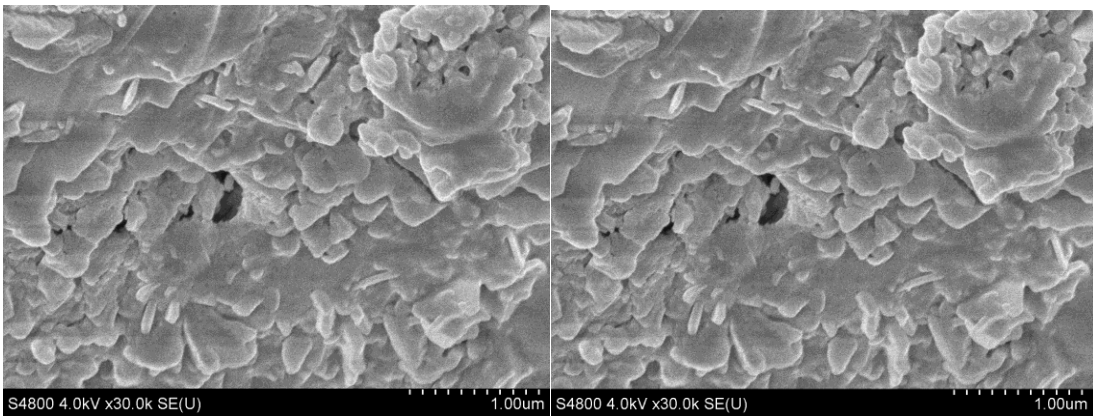

Figure S4. SEM images of Ru-ZIF-67-B and C. Related to Figure 1.

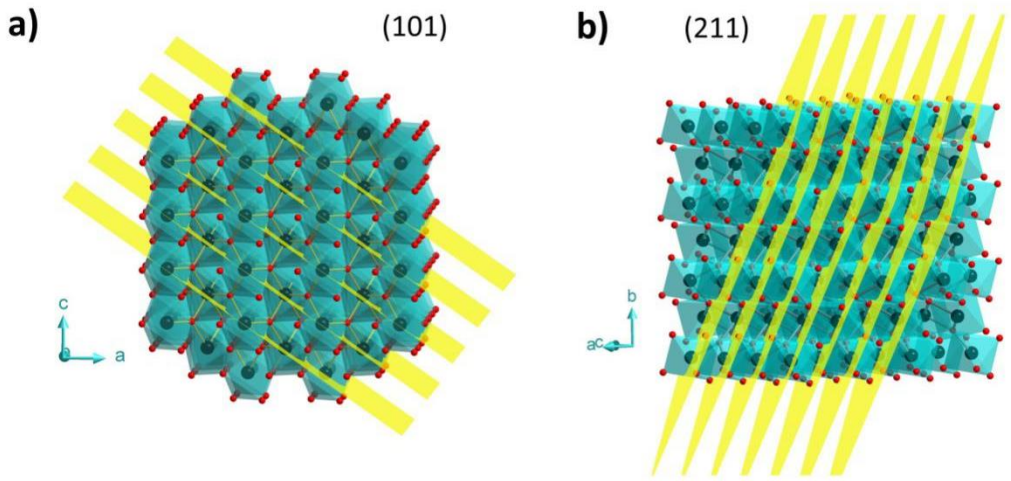

Figure S5. Crystal structure of RuO_2 viewed along different direction. The yellow planes represent the crystal facets of RuO_2. Related to Figure 1.

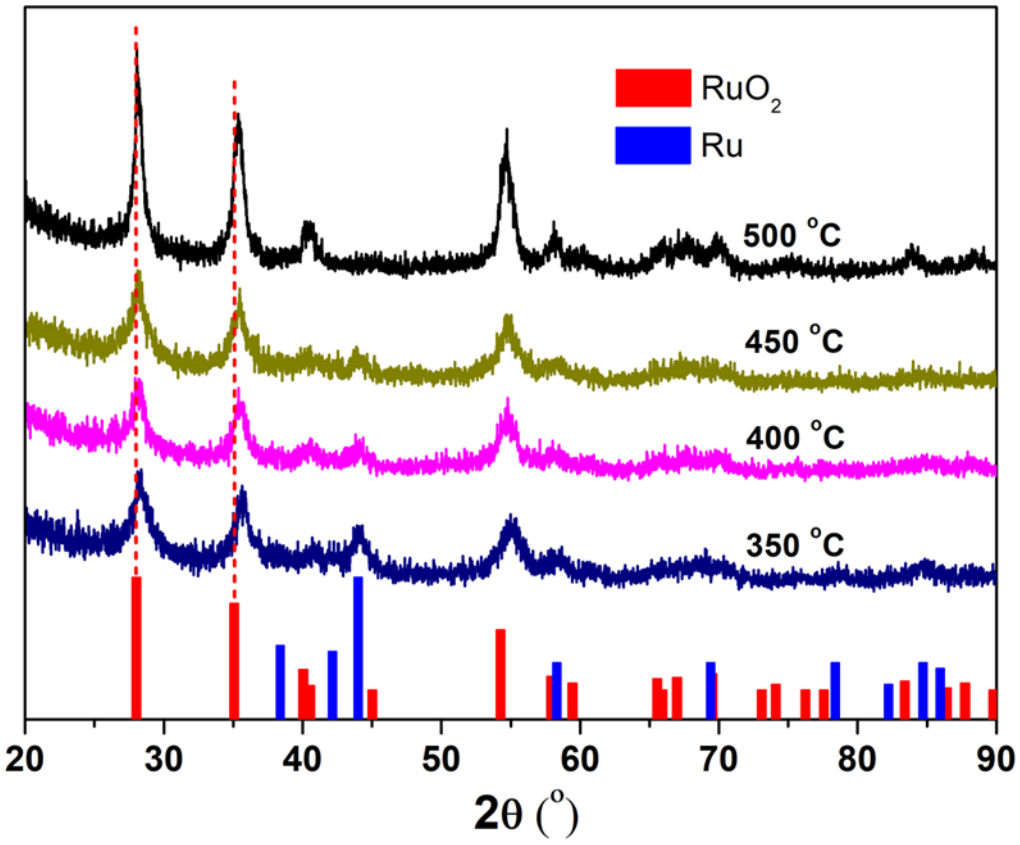

Figure S6. PXRD patterns of $Co_{0.11}Ru_{0.89}O_{2-\delta}$ annealed at different temperatures. Related to Figure 1.

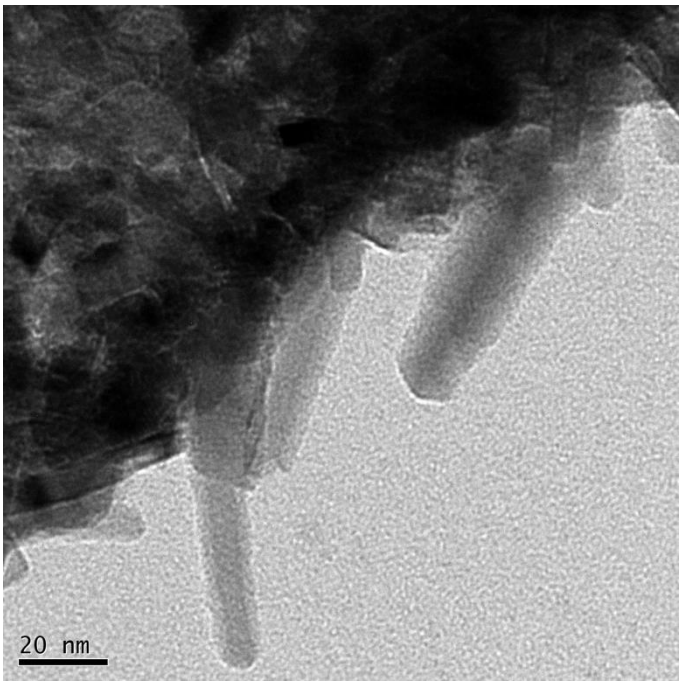

Figure S7. TEM image of $Co_{0.27}Ru_{0.73}O_{2-\delta}$ annealed at 350 ^{o}C . Related to Figure 2.

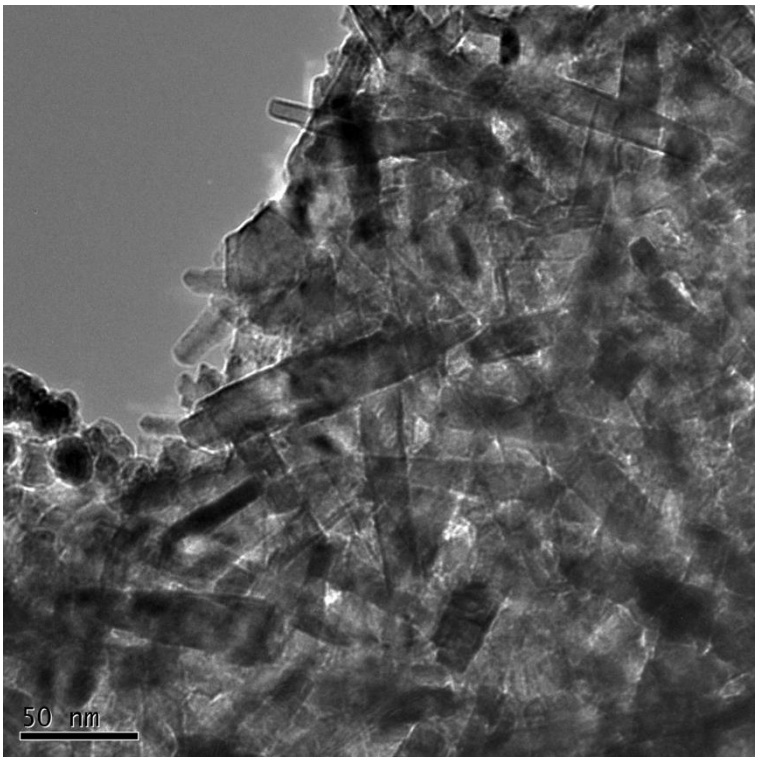

Figure S8. TEM image of $Co_{0.18}Ru_{0.82}O_{2-\delta}$ annealed at 350 ^{o}C . Related to Figure 2.

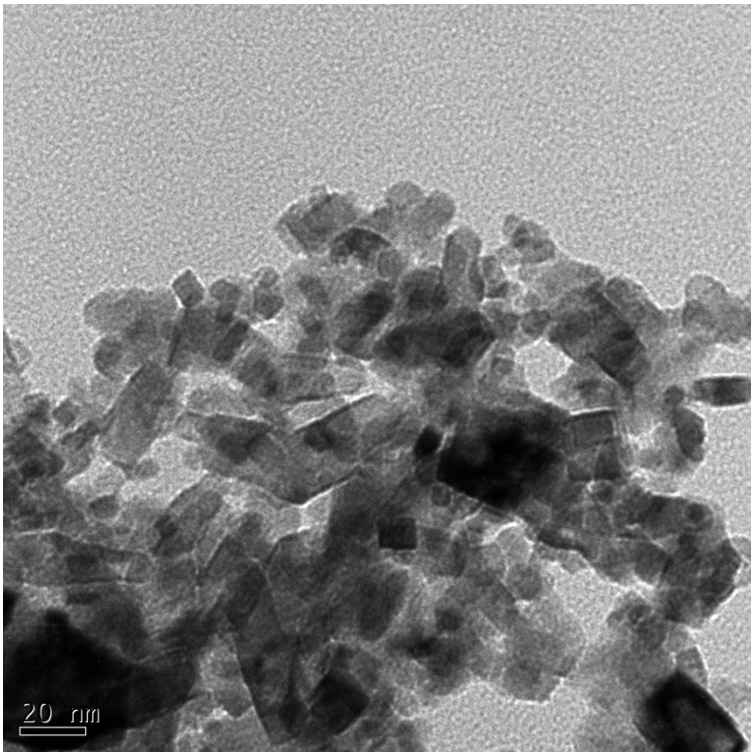

Figure S9. TEM image of $Co_{0.04}Ru_{0.96}O_{2-\delta}$ annealed at 350 ^{o}C . Related to Figure 2.

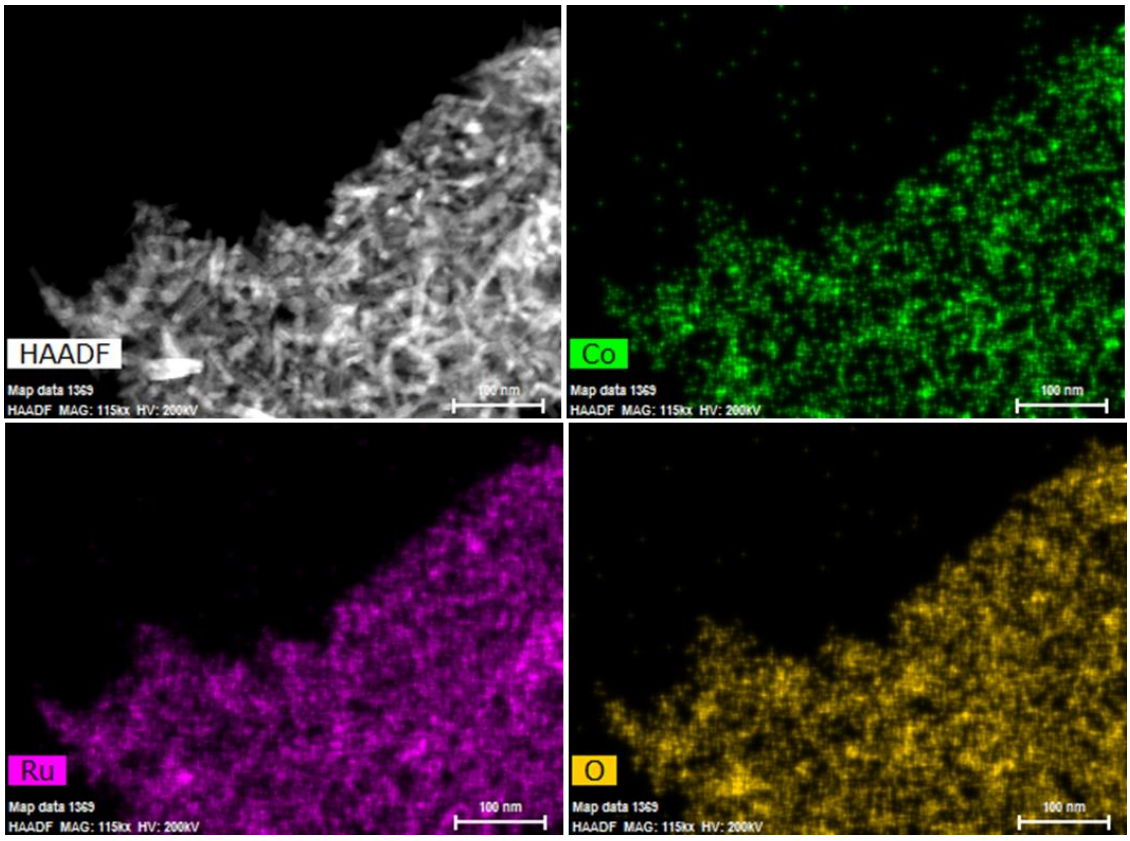

Figure S10. HAADF-STEM image and the corresponding element mapping images.

Related to Figure 2.

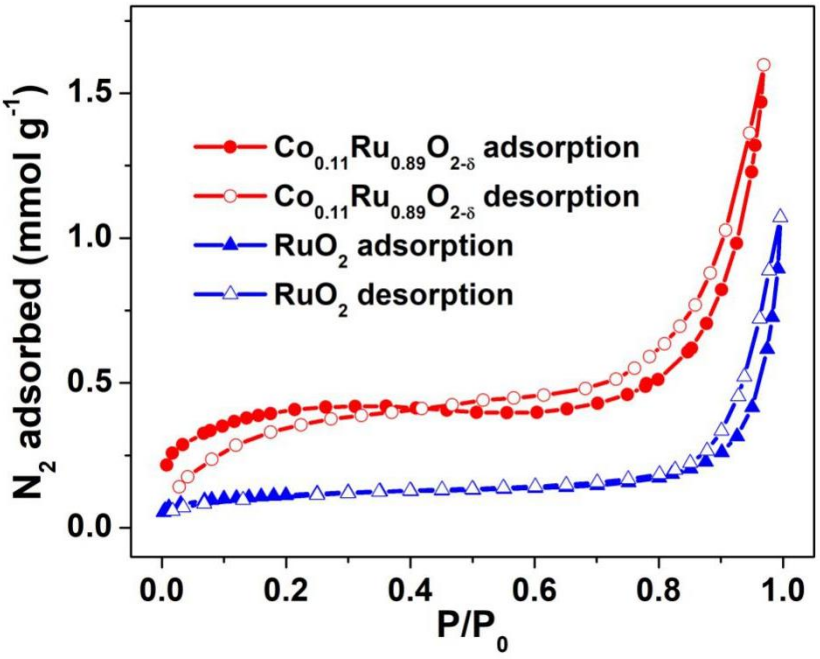

Figure S11. N_2 adsorption-desorption isotherms of $Co_{0.11}Ru_{0.89}O_{2-\delta}$(350) and RuO_2 at 77 K. Related to Figure 2.

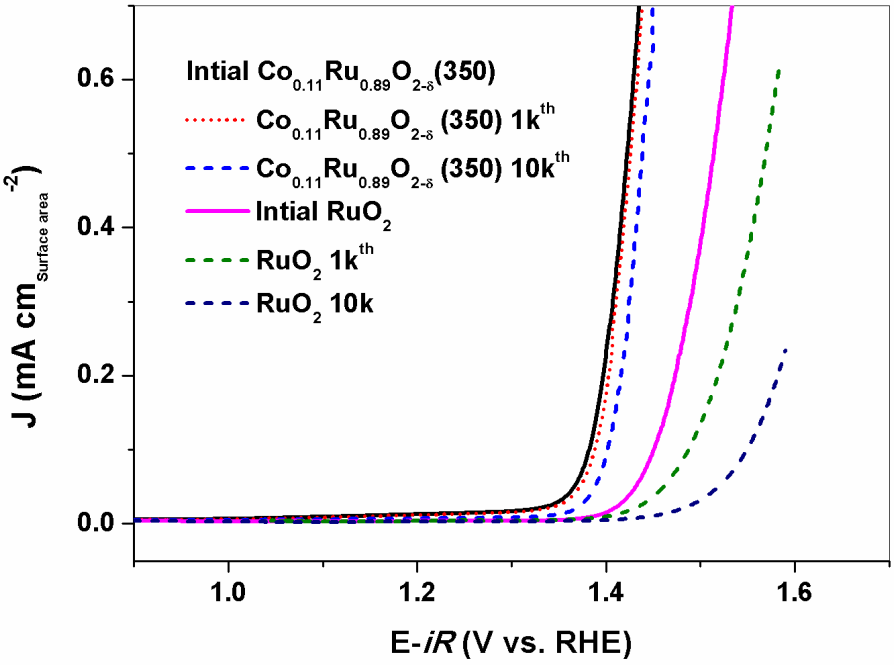

Figure S12. Intrinsic surface area based LSV curves of $Co_{0.11}Ru_{0.89}O_{2-\delta}$ (350) and commercial RuO_2 before and after CV cycling measurements. Related to Figure 3.

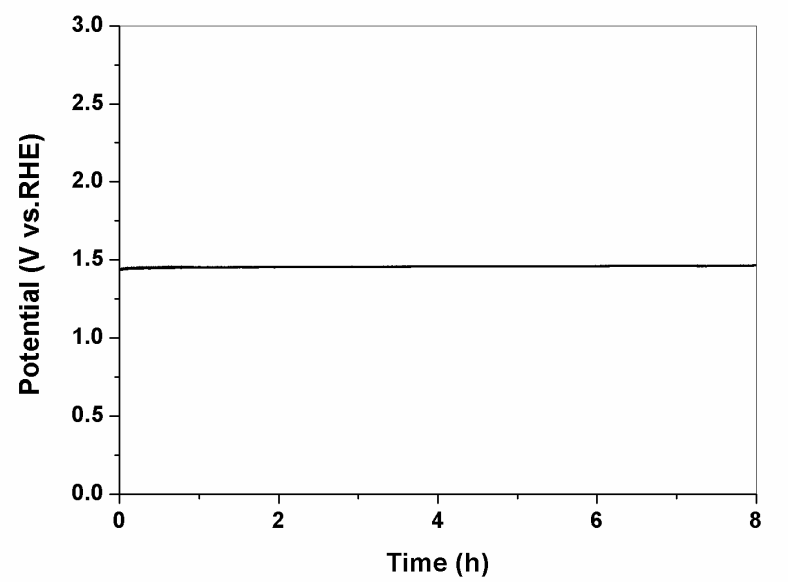

Figure S13. Chronopotentiometry test of $Co_{0.11}Ru_{0.89}O_{2-\delta}$ (350) at the current density of 50 mA cm^{-2}. Related to Figure 3.

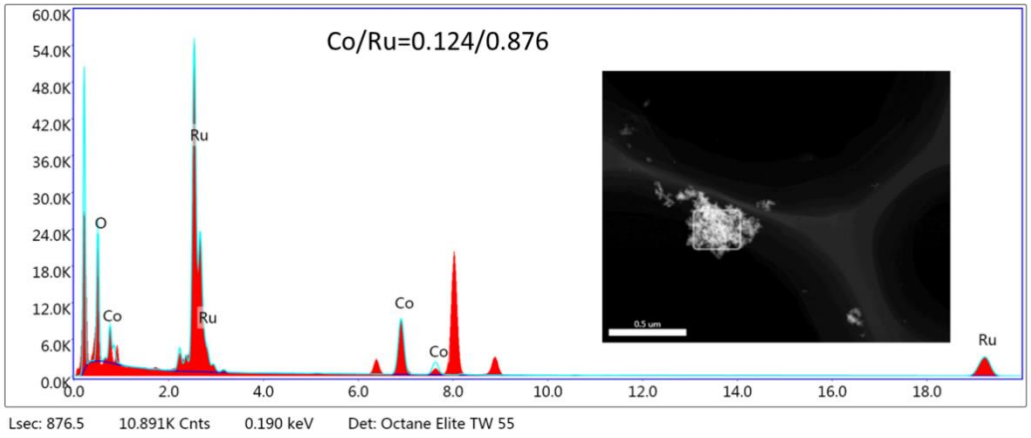

Figure S14. TEM-EDS of $Co_{0.11}Ru_{0.89}O_{2-\delta}$ (350) before stability test. Related to Figure 3.

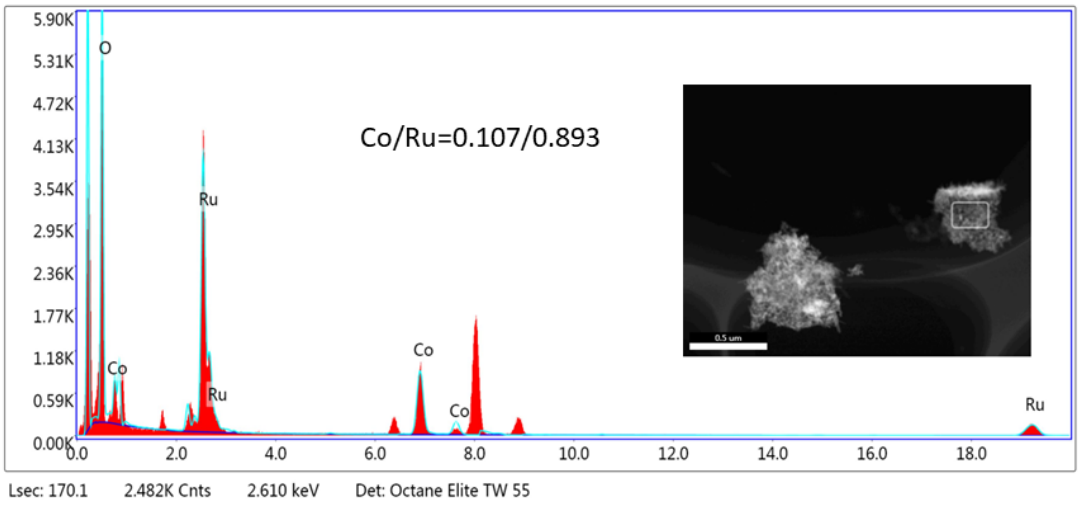

Figure S15. TEM-EDS of $Co_{0.11}Ru_{0.89}O_{2-\delta}$ (350) after stability test. Related to Figure 3.

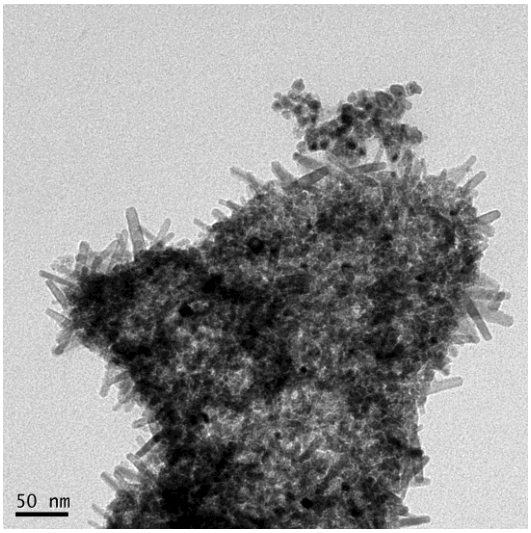

Figure S16. TEM image of f $Co_{0.11}Ru_{0.89}O_{2-\delta}$ (350) after stability test. Related to Figures 2 and 3.

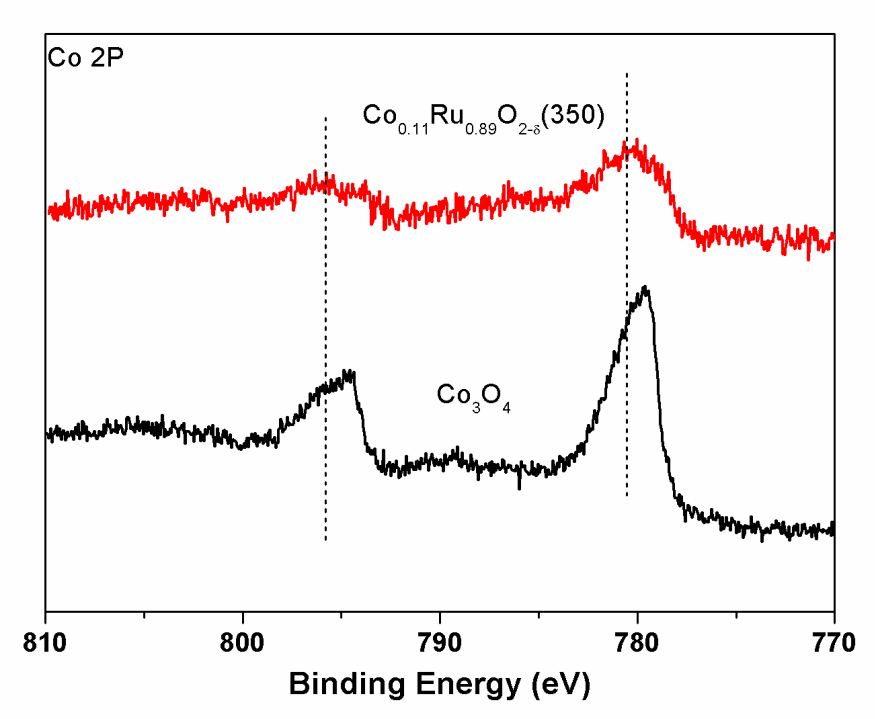

Figure S17. Co 2P XPS profiles of $Co_{0.11}Ru_{0.89}O_{2-\delta}$ and Co_3O_4. Co_3O_4 was synthesized by annealing pure ZIF-67 at 350 ^{o}C. Related to Figure 4.

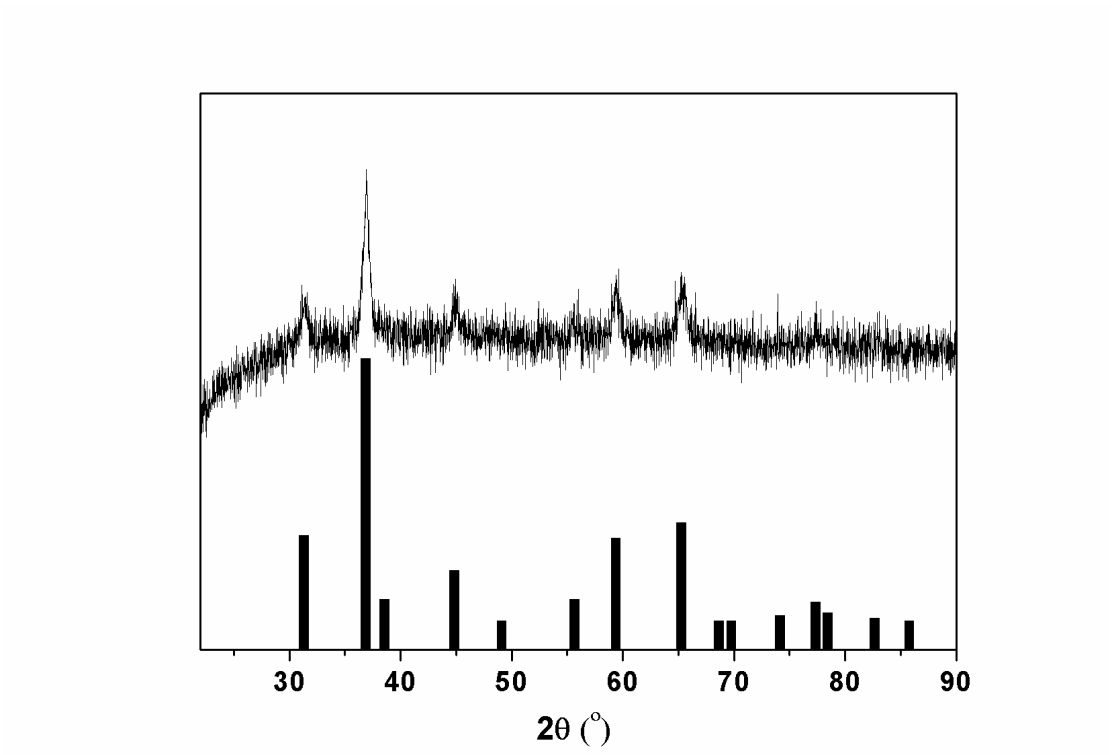

Figure S18. PXRD pattern of the product obtained from annealing pure ZIF-67. The reference patterns of Co_3O_4 were obtained from Jade 2004 (JCPDS No. 43-1003).

Related to Figure 4.

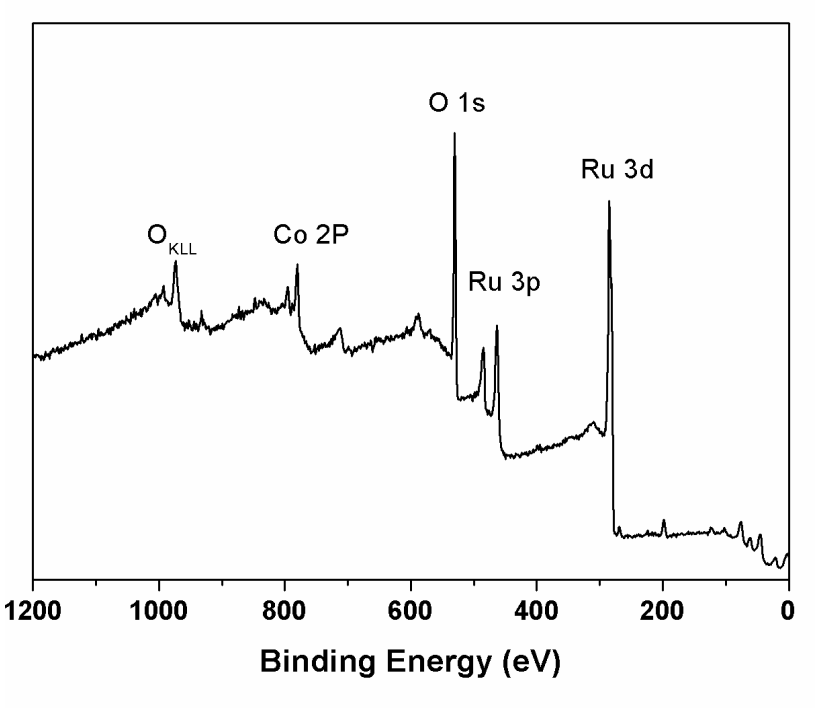

Figure S19. The XPS wide-scan spectra of $Co_{0.11}Ru_{0.89}O_{2-\delta}$(350). Related to Figure 4.

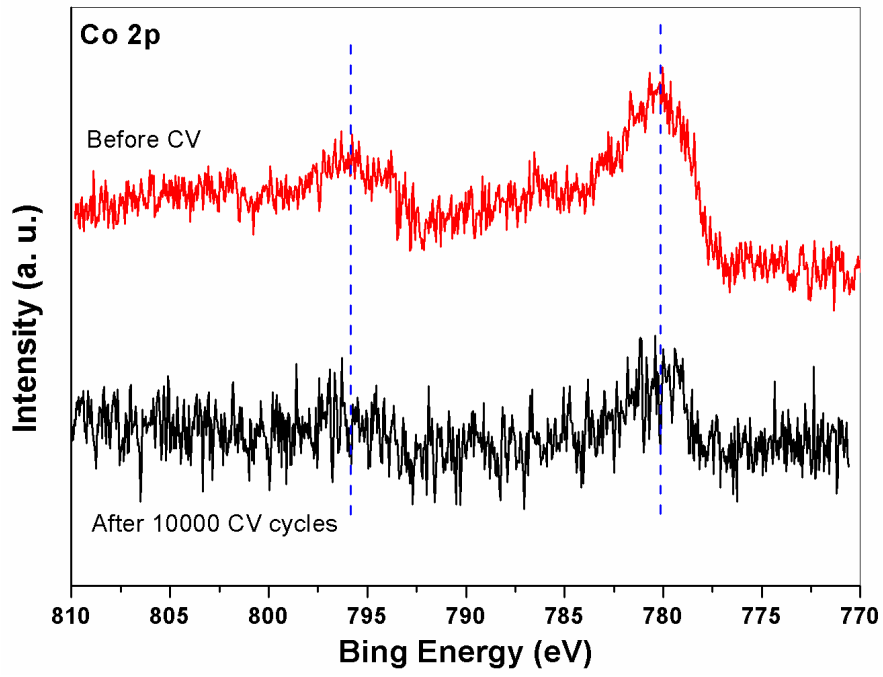

Figure S20. XPS spectra for Co of $Co_{0.11}Ru_{0.89}O_{2-\delta}$ (350) before and after 10000 CV cycles. Related to Figure 4.

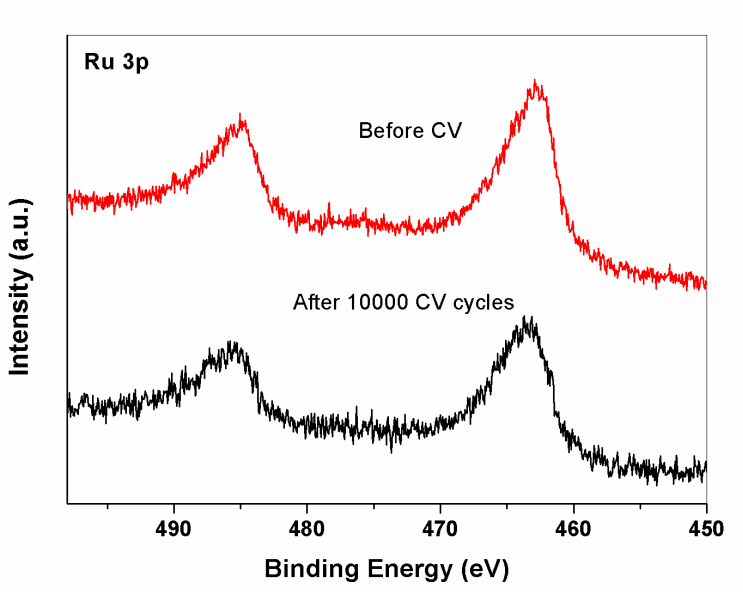

Figure S21. XPS spectra for Ru of $Co_{0.11}Ru_{0.89}O_{2-\delta}$ (350) before and after 10000 CV cycles. Related to Figure 4.

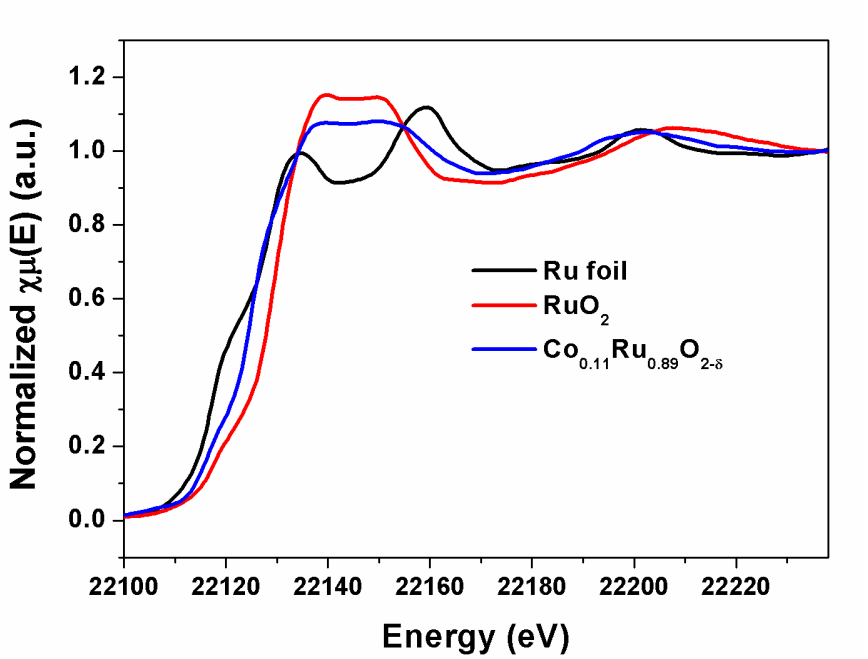

Figure S22. Normalized Ru K-edge XAS spectra of $Co_{0.11}Ru_{0.89}O_{2-\delta}$(350), RuO_2 and Ru foil. Related to Figure 4.

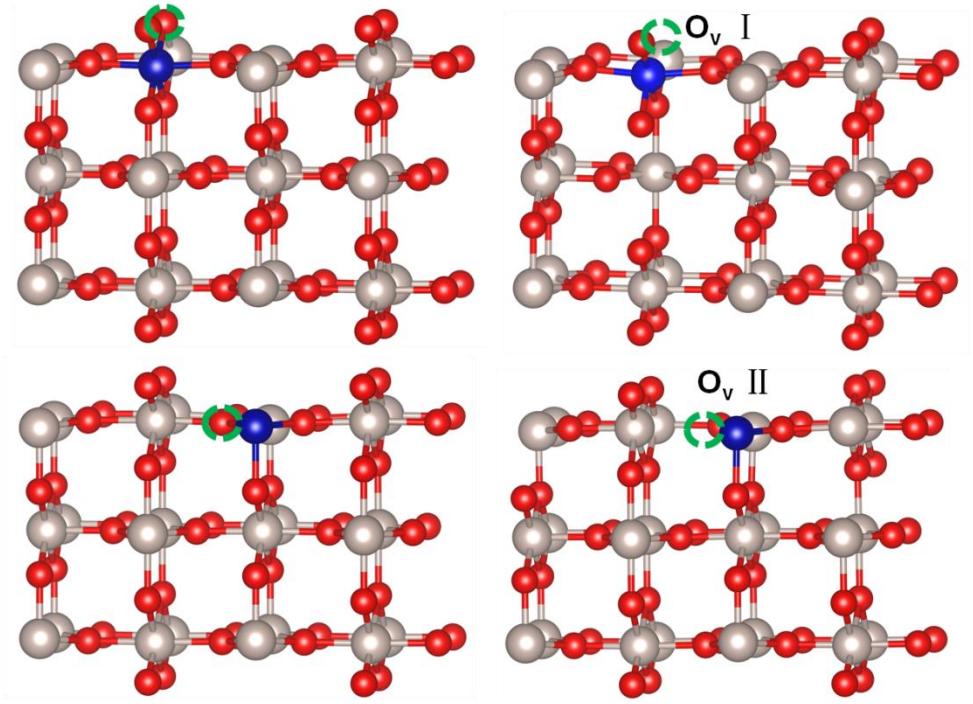

Figure S23. The formation of O vacancy for different Co doping sites. Related to Figure 5.

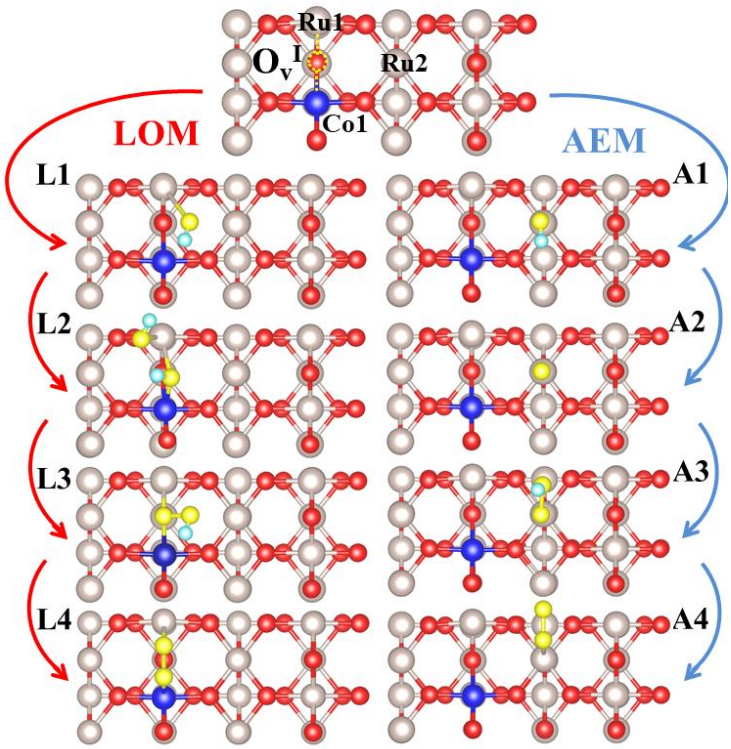

Figure S24. The intermediates along LOM and AEM processes. Related to Figure 5.

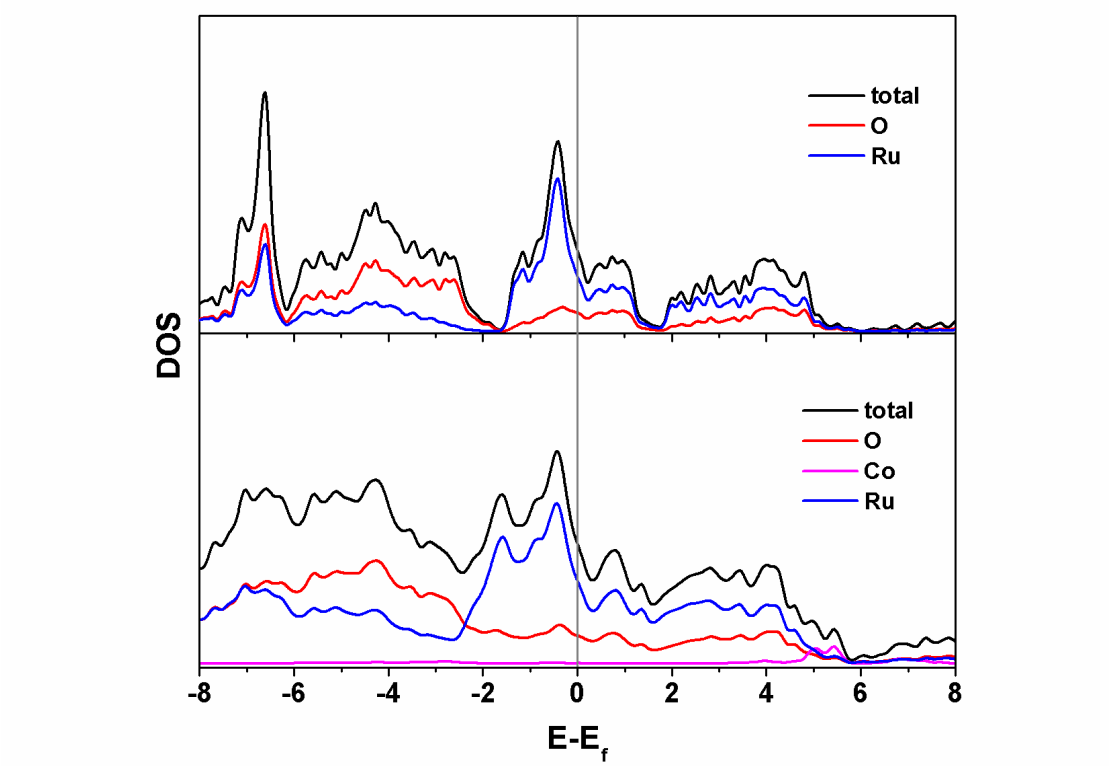

Figure S25. Calculated density of states (DOS) of bulk RuO_2 and Co-doped RuO_2. Related to Figure 5.

Table S1. The comparison of overpotentials of representative OER electrocatalysts in acidic media. Related to Figure 3.

Catalyst	substrate	Electrolyte	Overpotential at 10 mA cm^{-2} (mV)	Chronopotentiometry at specific current density	Ref.
Co-RuO_2	GCE	0.5 M H_2SO_4	169	50 h@10 mA cm^{-2}	**This work**
$Cr_{0.6}Ru_{0.4}O_2$(550)	GCE	0.5 M H_2SO_4	178	10 h @10 mA cm^{-2}	***Nat. Commun.*** *2019, 10:162*
Ba[Co-POM]	CP	1 M H_2SO_4	361	--	***Nat. Chem.*** *2018, 10, 24*
6H-IrO_2	GCE	0.5 M H_2SO_4	248	30 h @10 mA cm^{-2}	***Nat. Commun.*** *2018,9:5236*
IrCoNi PHNCs	GCE	0.1 M $HClO_4$	303	3.3 h@5 mA cm^{-2}	***Adv. Mater.*** *201, 729, 1703798,*
IrNiCu	GCE	0.1 M $HClO_4$	300	--	***ACS Nano.*** *2017,*

DNF					*11, 5500,*
Ir	GF	0.5 M H_2SO_4	290	10 h@10 mA cm^{-2}	***Nano Energy.*** *2017, 40, 27,*
$Ni_{0.5}Mn_{0.5}Sb_{1.7}Oy$	ATO	1 M H_2SO_4	~672	170 h@10 mA cm^{-2}	***Energy Environ. Sci.*** *2017, 10, 2103.*
$W_{0.57}Ir_{0.43}O_{3-\delta}$	FTO	1 M H_2SO_4	370	0.6 h@10 mA cm^{-2}	***Energy Environ. Sci.*** *2017, 10, 2432*
Co_3O_4	FTO	0.5 M H_2SO_4	570	12 h@10 mA cm^{-2}	***Chem. Mater.*** *2017, 29, 950*
$Y_2Ru_2O_{7-\delta}$	GCE	0.1 M $HClO_4$	270@1 mA cm^{-2}	8 h@1 mA cm^{-2}	***J. Am. Chem. Soc.*** *2017, 139, 12076*
IrO_2-RuO_2 @Ru	GCE	0.5 M H_2SO_4	281	--	***J. Mater. Chem. A*** *2017, 5, 17221*
NiFeP	Free-standing	0.05 M H_2SO_4	540	12 h@10 mA cm^{-2}	***Adv. Mater.*** *2017, 29. 1606570*
IrNi NCs	GCE	0.1 M $HClO_4$	280	2 h@5 mA cm^{-2}	***Adv. Func. Mater.*** *2017. 27, 1700886*
Co-IrCu ONC	GCE	0.1 M $HClO_4$	290	--	***Adv. Func. Mater .****2017, 27, 1604688*
IrO_x-Ir	GC plates	0.5 M H_2SO_4	290	100 h@2 mA cm^{-2}	***Angew. Chem. Int. Ed.*** *2016, 55, 752*
$IrO_x/SrIrO_3$	$SrTiO_3$	0.5 M H_2SO_4	270-290	30 h@10 mA cm^{-2}	***Science.*** *2016, 353, 1011*
$BaYIrO_6$	Au	0.1 M H_4ClO_4	~315	1 h@10 mA cm^{-2}	***Nat. Commun.*** *2016, 7, 12363*
Ir-Ni Oxide	Ti	0.1 M HClO4	~270	--	***J. Am. Chem. Soc.*** *2015, 137, 13031*
$IrNiO_x$	ATO	0.05 M H_2SO_4	~330	--	***Angew. Chem. Int. Ed.*** *2015, 54, 2975*
IrO_2	GCE	0.1 M H_4ClO_4	~430	--	***J. Electrochem. Soc.*** *1983, 130, 825*

Transparent Methods

Materials. All reagents are of analytical grade and used as received. The commercial RuO_2 and Nafion (5 wt% soluton) were purchased from Sigma-Aldrich.

Synthesis of ZIF-67. The ZIF-67 nanoparticles were synthesized via a procedure reported in literature. Cobalt nitrate hexahydrate (0.3 g) and 2-methylimidazole (0.66 g) were dissolved in methanol (11.3 g). The two solutions were then mixed and stirred at room temperature at 600 rpm for 24 h. The resulting purple precipitate was separated from the solution by centrifugation at 4000 rpm for 10 minutes and washed three times with methanol and dried overnight at 80 ^{o}C. The sample was further dried at 100 ^{o}C under vacuum for 12 h for future use.

Synthesis of Ru-ZIF-67. Typically, ZIF-67 (0.1 g) powder and desired amount of $RuCl_3 \cdot xH_2O$ were added into 15 mL tetrahydrofuran (THF) and allowed to stir for 24 h. The resulting precipitate was centrifuged and washed with 3 times with THF, then dried at 80 ^{o}C in air. To obtain different Ru content Ru-ZIF-67, the amount of $RuCl_3 \cdot xH_2O$ added was 0.2 g, 0.3 g, 0.4 g and 0.6 g respectively. For clearness, we denoted these samples as Ru-ZIF-67-A, Ru-ZIF-67-B, Ru-ZIF-67-C, and Ru-ZIF-67-D, respectively.

Synthesis of Co-doped RuO_2 nanorods. Co-doped RuO_2 powders were obtained by annealing Ru-ZIF-67 precursors in air at temperatures of 300~500 ^{o}C for 4 h. Typically, 20 mg of Ru-ZIF-67-C were placed in crucible and put into a muffle, and then annealed in air with a heating rate of 10 ^{o}C min^{-1} to 350 ^{o}C, and held at 350 ^{o}C for 4 h.

Characterizations. Powder X-ray diffractions (PXRD) characterization of the samples were performed on a D8-Advance Bruker AXS diffractometer with $Cu_{K\alpha}$ (λ=1.5418 Å)

radiation at a voltage of 40 kV and 40 mA. The sample morphologies were characterized using a field-emission scanning electron microscope (SEM) (Hitachi, S-4800). SEM specimens were prepared by depositing sample powders onto carbon adhesive tapes. Transmission electron microscopy (TEM) images and high-angle annular dark-field scanning transmission electron microscopy (HAADF-STEM) images were carefully recorded on Talos F200X and JEM-ARM200F. The chemical composition and bonding states were measured by X-ray photoelectron spectroscopy (XPS) using a Kratos AXIS ULTRA^{DLD} instrument with a monochromic Al-Kα X-ray source (hν=1496.6 eV). The power was 120 W and the X-ray spot size was set to 700×300 μm. The pass energy of the XPS analyzer was set as 20 eV. The base pressure of the analysis chamber was better than 5×10^{-9} Torr. The nitrogen adsorption-desorption isotherm was measured on ASAP 2020M apparatus at 77 K. Before the measurements, the samples were outgassed under vacuum at 160 ^{o}C for 12 hours. Raman spectra were recorded on a Renishaw inVia Reflex spectrometer. Inductively coupled plasma-mass spectroscopy (ICP-MS) measurements were carried on NexION 300 (Perkin-Elmer).

Electrochemical measurements. In a typical procedure, 4 mg of Co-RuO_2 powder was added to 1 mL of water/ethanol (3:1, v/v) containing 15 μL Nafion aqueous solution (5%, Sigma-Aldrich), and dispersed by sonication under shaking for 30 min to generate a homogeneous black ink. 5 μL of the prepared catalyst ink was drop-cast on a glassy carbon electrode (Geometric area: 0.07065 cm^2) and dried at room temperature to form a thin film working electrode. A three-electrode system, contained a glassy carbon working electrode, a counter electrode made of platinum wire (diameter: 0.5 nm), and a saturated Hg/Hg_2SO_4

reference electrode, were used to measure the electrochemical properties. All measurements were performed in 0.5 M H_2SO_4 acidic solution. The Hg/Hg_2SO_4 reference electrode was calibrated with a Pt wire electrode in H_2-satured 0.5 M H_2SO_4 solution. The results showed that the potential difference between the Hg/Hg_2SO_4 reference electrode and reversible hydrogen electrode was 0.645 V. Cyclic voltammograms (CVs) tests were collected at a scan rate of 100 mV s^{-1} typically between 1.2 and 1.6 V. Chronopotentiometric measurements were carried out by applying a constant current of 10 mA cm^{-2} for up to 50 h. Electrochemical impedance spectroscopy (EIS) were performed at 1.4 V. The EIS results were presented in the form of Nyquist plot and fitted using ZView software with a representative equivalent electrical circuit. We carried out iR correction according to the literatures reported.[Zheng et al. 2017; Li et al. 2017] The potential was manually corrected using Ohm's law: $E=E_{app}-iR_s*0.85$, where Rs (solution resistance) is determined to be 9 Ω by EIS (Figure 3c).

Calculation details

All DFT calculations are carried out by using the Vienna ab-initio Simulation Package (VASP) [Kresse, et al. 1996] to optimize geometry structures and energies. The exchange–correlation functional is performed within the generalized gradient approximation proposed by Perdew–Burke–Ernzerh (GGA-PBE).[Perdew, et al. 1996; Perdew, et al. 1992;] The core electrons is described by the Projector Augmented Wave (PAW) potential,[Blochl, et al. 1994] and the cut-off kinetic energies for the plane waves are set to 500 eV.[Kresse, et al. 1994] The convergence criteria of energy and force on each atom after relaxation are less than 10^{-4} eV

and 0.02 eV/A˚, respectively. The RuO_2(110) is built with 2*2 supercell with fixing two bottom layers in the geometry optimization. The Brillouin zone is sampled by Gamma point [Hendrik, et al. 1976] and a vacuum distance of 15 Å along z direction was set to ensure sufficient vaccum on surface. The Thermal and zero point energy (ZPE) corrections are further calculated by DFT-D3 to obtain the Gibbs free energy (ΔG), which is determined following ΔG = ΔE + ΔEZPE – TΔS, according to the standard hydrogen electrode (SHE) model proposed by Nørskov et al.[Peterson, et al. 2010] Grimme's DFT-D3 scheme are expected to provide dispersion correction in van der Waals (vdW) interactions.[Grimme, et al. 2010; Grimme, et al. 2011] ΔE, ΔEZPE and ΔS are the electronic total energy differences, the differences in the zero point energy and the change of entropy, respectively. T is the temperature set to 298.15 K.

Free energy calculations: The Gibbs free energy changes are calculated by the following equations (1) to (4) for AEM while those for LOM are calculated by the equations (5) to (8) [Rossmeisl, et al. 2005].

$$\Delta G_1=\Delta G_{O^*}-\Delta G_{OH^*}-eU+\Delta G_{H^+}\ (pH) \quad (1)$$

$$\Delta G_2=\Delta G_{OOH^*}-\Delta G_{O^*}-eU+\Delta G_{H^+}\ (pH) \quad (2)$$

$$\Delta G_3=\Delta G_{OO^*}-\Delta G_{OOH^*}-eU+\Delta G_{H^+}\ (pH) \quad (3)$$

$$\Delta G_4=4.92eV+\Delta G_{OH^*}-\Delta G_{OO^*}-eU+\Delta G_{H^+}\ (pH) \quad (4)$$

$$\Delta G_1=\Delta G_{[Ov\text{-}OH]^*}-\Delta G_{[Ov\text{-}OO]^*}-eU+\Delta G_{H^+}\ (pH) \quad (5)$$

$$\Delta G_2=\Delta G_{[OH+Ov\text{-}OH)]^*}-\Delta G_{[Ov\text{-}OOH]^*}-eU+\Delta G_{H^+}\ (pH) \quad (6)$$

$$\Delta G_3=\Delta G_{[Ov\text{-}OOH)]^*}-\Delta G_{[OH+Ov\text{-}OH)]^*}-eU+\Delta G_{H^+}\ (pH) \quad (7)$$

$$\Delta G_4 = 4.92eV + \Delta G_{[Ov\text{-}OO]^*} - \Delta G_{[Ov\text{-}OOH)]^*} - eU + \Delta G_{H^+}(pH) \quad (8)$$

where U is the potential determined against by normal hydrogen electrode (NHE) at standard condition (T = 298.15 K, P = 1 bar, pH = 0)[Nørskov et al. 2004]. The free energy changes of the protons relative to the above-specified electrode at non-zero pH is represented by Nernst equation as $\Delta G_{H^+}(pH) = -k_B T \ln(10) \times pH$. The Gibbs free energy differences of these intermediates include zero-point energy (ZPE) and entropy corrections according to $\Delta G = \Delta E + \Delta ZPE - T\Delta S$, where the energy differences ΔE are calculated with respect to H_2O and H_2 (at U = 0 and pH = 0). The theoretical overpotential is defined as the lowest potential at which all reaction steps are thermodynamically downhill.[Man, et al. 2011; Doyle, et al. 2015]

References

Blochl, P. E. (1994). Projector augmented-ware method. Phys. Rev. B. *50*, 27.

Doyle, A. D., Montoya, J. H., Vojvodic, A. (2015) Improving oxygen electrochemistry through nanoscopic confinement. ChemCatChem ***7***, 738.

Grimme, S., Antony, J., Ehrlich, S., Krieg, H. (2010). A consistent and accurate ab initio parametrization of density functional dispersion correction (DFT-D) for the 94 elements H-Pu. J. Chem. Phys. *132*, 154104.

Grimme, S., Ehrlich, S., Goerigk, L. (2011). Effect of the Damping Function in Dispersion Corrected Density Functional Theory. J. Comput. Chem. *32*, 1456.

Hendrik, J., Ma, J. (1976). Special points for Brillouin-zone integratiionns. Phys Rev B. *13*, 5.

Kresse, G., Furthmuller, J. (1996). Efficient iterative schemes for *ab* initio total-energy calculations using a plane-wave basis set. Phys. Rev. B *54*, 11169-11186.

Li, Y., Cui, F., Ross, M.B., Kim, D., Sun, Y., Yang, P. (2017). Structure-sensitive CO_2 electroreduction to hydrocarbons on ultrathin 5-fold twinned copper nanowires. Nano Lett. *17*, 1312-1317.

Man I. C. et al. (2011). Universality in oxygen evolution electrocatalysis on oxide surfaces. ChemCatChem, *3*, 1159.

Nørskov J. K. et al. (2004). Origin of the overpotential for oxygen reduction at a fuel-cell cathode. J. Phys.Chem. B *108*, 17886.

Perdew, J.P., Burke, K., Ernzerhof, M. (1996). Generalized gradient approximation made simple. Phys. Rev. Lett. *77*, 3865.

Perdew J.P., Wang Y. (1992). Pair-distribution function and its coupling-constant average for the spin-polarized electron gas. Phys. Rev. B: Condens Matter. *46*, 12947.

Peterson, A. A., Abild-Pedersen, F., Studt, F., Rossmeisl, J., Norskov, J. K. (2010). How copper catalyzes the electroreduction of carbon dioxide into hydrocarbon fuels. Energy Environ. Sci. *3*, 1311.

Rossmeisl, J., Logadottir, A., Nørskov J.K. (2005). Electrolysis of water on (oxidized) metal surfaces, Chem. Phys. *319*, 178.

Zheng, X., et al (2017). Sulfur-modulated tin sites enable highly selective electrochemical reduction of CO_2 to format. Joule, *1*, 794–805.